

1 INTRODUCTION

2 Above Earth's atmosphere are the Van Allen radiation belts, a toroidally-shaped
3 pair of belts that consist of a complex and dynamic plasma environment. The inner
4 radiation belt consists of mostly energetic protons, is very stable on year time scales,
5 and is located within 2 Earth radii (measured near the equator) above Earth's Earth's
6 surface. The outer radiation belt, on the other hand, consists of mostly energetic
7 electrons, is highly dynamic on day, and even hour time scales, and is typically
8 found between 4 and 8 Earth radii above Earth's surface. The radiation belts pose a
9 challenge to space exploration due to their effects on our technology-driven society.
10 Some of the effects include: a higher radiation dose for astronauts and cosmonauts,
11 degradation of silicon to the point where transistors malfunction, computer memory
12 corrupts due to bit flips, etc. With these effects in mind, it is no surprise that the
13 radiation belts have been extensively studied since their discovery in the 1960s.

14 The radiation belt plasma is at times unstable which in turn generate electric and
15 magnetic waves. These waves in turn accelerate and scatter radiation belt particles
16 with a variety of wave-particle mechanisms. One form of wave-particle interactions
17 scatter particles into Earth's atmosphere in the form of electron microbursts.

18 Electron microbursts, henceforth referred to as microbursts, are typically
19 observed by low Earth orbiting spacecraft, sounding rockets, and high altitude
20 balloons as a sub-second impulse of electrons. Some of the most intense microbursts
21 have electron fluxes that are a factor of 10 to 100 above the background (for example
22 see Fig. 7 in Blake et al. (1996)). Since they were first reported by Anderson and
23 Milton (1964), the intense transient nature of microbursts have compelled countless
24 researchers to understand their properties, their effects on the environment, and the
25 physical mechanism(s) that create microbursts. Microbursts are widely believed

26 to be created by wave-particle scattering between a plasma wave called whistler
 27 mode chorus and outer radiation belt electrons, although many details regarding the
 28 scattering mechanism are unconstrained or unknown. The goal of this dissertation is
 29 to study the wave-particle scattering mechanism that scatters electron microbursts.

30 This chapter serves as an introduction to the fundamental physical concepts
 31 that are essential to understand wave-particle interactions in Earth's magnetosphere.
 32 We will first derive the motion of individual charged particles in Earth's electric and
 33 magnetic fields. Next we will cover how various groups of charged particles coalesce
 34 to form the major particle populations in the magnetosphere. Then, we will cover
 35 the various mechanisms that accelerate and scatter particles in the magnetosphere.
 36 Lastly, we will review microbursts, which is one of the loss mechanism, as a jumping-
 37 off point for the rest of the dissertation.

38 Charged Particle Motion in Electric and Magnetic Fields

A charged particle trapped in the magnetosphere will experience three types
 of periodic motion in Earth's nearly dipolar magnetic field. The three motions are
 ultimately due to the Lorentz force that a particle of momentum \vec{p} , charge q , and
 velocity \vec{v} experiences in an electric field \vec{E} and magnetic field \vec{B} and is given by

$$\frac{d\vec{p}}{dt} = q(\vec{E} + \vec{v} \times \vec{B}). \quad (1.1)$$

39 In the magnetosphere, the three periodic motions, in decreasing frequency, are
 40 gyration, bounce, and drift and are schematically shown in Fig. 1.1. Each periodic
 41 motion has a corresponding conserved quantity i.e. an adiabatic invariant.

The highest frequency periodic motion is gyration about a magnetic field of

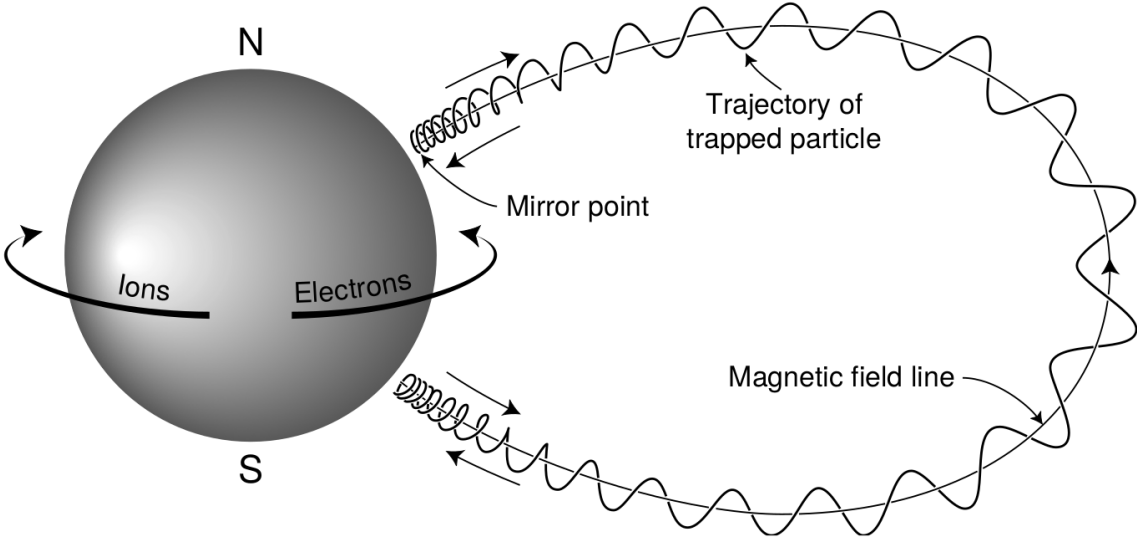


Figure 1.1: The three periodic motions of charged particles in Earth's dipole magnetic field. These motions are: gyration about the magnetic field line, bounce motion between the magnetic poles, and azimuthal drift around the Earth. Figure from (Baumjohann and Treumann, 1997).

magnitude B . This motion is circular with a Larmor radius of

$$r = \frac{mv_{\perp}}{|q|B} \quad (1.2)$$

where m is the mass and v_{\perp} the particle's velocity perpendicular to \vec{B} . This motion has a corresponding gyrofrequency

$$\Omega = \frac{|q|B}{m} \quad (1.3)$$

in units of radians/second. In the radiation belts, the electron gyrofrequency, Ω_e is on the order of a kHz. The corresponding adiabatic invariant is found by integrating the particle's canonical momentum around the particle's path of gyration

$$J_i = \oint (\vec{p} + q\vec{A}) \cdot d\vec{l} \quad (1.4)$$

42 where J_i is the i^{th} adiabatic invariant and \vec{A} is the magnetic vector potential. This
 43 integral is carried out by integrating the first term over the circumference of the
 44 gyro orbit and integrating the second term using Stokes theorem to calculate the
 45 magnetic flux enclosed by the gyro orbit. The gyration invariant is $J_1 \sim v_{\perp}^2/B$, which
 46 is conserved when the frequency, ω of a force acting on the gyrating electron satisfies
 47 $\omega \ll \Omega_e$.

48 The second highest frequency periodic motion is bouncing due to a parallel
 49 gradient in \vec{B} . This periodic motion naturally arises in the magnetosphere because
 50 Earth's magnetic field is stronger near the poles, and artificially in the laboratory
 51 in magnetic bottle machines. To understand this motion we first we need to define
 52 the concept of pitch angle, α as the angle between \vec{B} and \vec{v} which is schematically
 53 shown in Fig. 1.2a. The pitch angle relates v with v_{\perp} , and v_{\parallel} (the component of the
 54 particles velocity parallel to \vec{B}). As shown in Fig. 1.2b and 1.2c, a smaller (larger)
 55 α will increase (decrease) the distance that the charged particle travels parallel to \vec{B} ,
 56 during one gyration.

Assuming the particle's kinetic energy is conserved, the conservation of J_1
 implies that given a particle's $v_{\perp}(0)$ and $B(0)$ at the magnetic equator (where
 Earth's magnetic field is usually at a minimum), we can calculate its $v_{\perp}(s)$ along the
 particle's path s by calculating $B(s)$ from magnetic field models. Thus the particle's
 perpendicular velocity is then related via

$$\frac{v_{\perp}^2(0)}{B(0)} = \frac{v_{\perp}^2(s)}{B(s)} \quad (1.5)$$

57 which can be rewritten as

$$\frac{v^2 \sin^2 \alpha(0)}{B(0)} = \frac{v^2 - v_{\parallel}^2(s)}{B(s)} \quad (1.6)$$

⁵⁸ and re-arranged to solve for $v_{||}(s)$

$$v_{||}(s) = v \sqrt{1 - \frac{B(s)}{B(0)} \sin^2 \alpha(0)} \quad (1.7)$$

⁵⁹ which will tend towards 0 when the second term in the radical approaches 1.

⁶⁰ The location where $v_{||}(s) = 0$ is called the mirror point and is where a particle
⁶¹ reverses direction. Since Earth's magnetic field is stronger towards the poles, the
⁶² mirroring particle will execute periodic bounce motion between its two mirror points
⁶³ in the northern and southern hemispheres. The corresponding adiabatic invariant, J_2
⁶⁴ is

$$J_2 = \oint p_{||} ds \quad (1.8)$$

where ds describes the particle path between the mirror points in the northern and southern hemispheres (see Fig. 1.1). J_2 is found by substituting Eq. 1.7 into Eq. 1.8 and defining the magnetic field strength at the mirror points as B_m (where $\alpha(m) = 90^\circ$). The J_2 integral can be written as

$$J_2 = 2p \int_{m_n}^{m_s} \sqrt{1 - \frac{B(s)}{B(m)}} ds \quad (1.9)$$

⁶⁵ where m_n and m_s are the northern and southern mirror points, respectively. The
⁶⁶ bounce period can be estimated (e.g. Baumjohann and Treumann, 1997) to be

$$t_b \approx \frac{LR_e}{\sqrt{W/m}} (3.7 - 1.6 \sin \alpha(0)) \quad (1.10)$$

⁶⁷ where W is the particle's kinetic energy, and L is the L -shell. L -shell describes the
⁶⁸ distance from the Earth's center to the location where a particular magnetic field
⁶⁹ line crosses the magnetic equator, in units of Earth radii, R_e . As with gyration, the

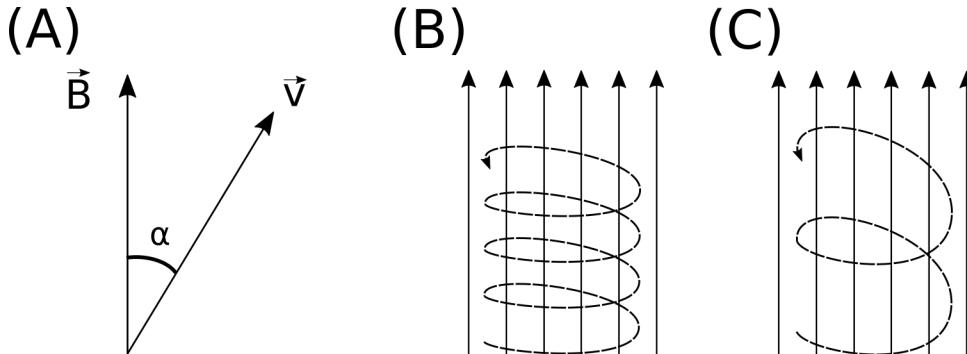


Figure 1.2: Charged particle motion in a uniform magnetic field \vec{B} . Panel (A) shows the geometry defining the pitch angle, α . Panel (B) and (C) show two helical electron trajectories with dashed lines assuming a large and small α (corresponding to a small and large parallel velocity $v_{||}$), respectively.

70 particle will bounce between the mirror points as long as $\omega \ll \Omega_b$, where Ω_b is the
71 bounce frequency.

72 At this stage it is instructional to introduce the notion of the loss cone pitch
73 angle, α_L . A particle with $\alpha \leq \alpha_L$ will mirror at or below ≈ 100 km altitude in
74 the atmosphere. A charged particle gyrating at those altitudes will encounter and
75 Coulomb scatter with the dense atmosphere and be lost from the magnetosphere.

76 The slowest periodic motion experienced by charged particles in Earth's mag-
77 netic field is azimuthal drift around the Earth. This drift results from a combination of
78 a radial gradient in \vec{B} and the curvature of the magnetic field. The radial gradient drift
79 arises because Earth's magnetic field is stronger near the Earth where the particle's
80 gyroradius radius of curvature shrinks as it gyrates towards stronger magnetic field,
81 and expands when it gyrates outward. The overall effect is the particle gyro orbit does
82 not close on itself and negatively charged particles drift east and positively charged
83 particles drift west. The radial gradient drift is further enhanced by the centrifugal
84 force that a particle experiences as it bounces along the curved field lines. The drift
85 adiabatic invariant, J_3 is found by integrating Eq. 1.4 over the complete particle orbit

86 around the Earth. The shape of this drift orbit is known as a drift shell. For J_3 , the
 87 first term is negligible and the second term is the magnetic flux enclosed by the drift
 88 shell, Φ_m i.e. $J_3 \sim \Phi_m$.

89 Figure 1.3 from Schulz and Lanzerotti (1974) shows contours of the gyration,
 90 bounce, and drift frequencies for electrons and protons in Earth's dipole magnetic
 91 field.

Up until now we have considered the three periodic motions due Earth's magnetic field in the absence of electric fields. If there is an electric field, E_\perp perpendicular to \vec{B} , a particle's center of gyration i.e., averaged position of the particle over a gyration, will drift with a velocity perpendicular to both E_\perp and \vec{B} . The drift velocity can be solved using Eq. 1.1 and is

$$\vec{v}_E = \frac{\vec{E} \times \vec{B}}{B^2}. \quad (1.11)$$

92 If there is a parallel magnetic field, $E_{||}$ then the particle is accelerated along the
 93 magnetic field line. An $E_{||}$ pointing away from the Earth will contribute to the mirror
 94 force and raise the particle's mirror point. On the contrary, an Earthward pointing
 95 $E_{||}$ will oppose the mirror force and lower the mirror point. If the Earthward $E_{||}$ is
 96 strong enough, the mirror point is lowered into the atmosphere that will precipitate
 97 particles. This is the mechanism that generates the aurora.

98 Particle Populations and Their Interractions in the Magnetosphere

99 Now that we have looked at the dynamics of single-particle motion in electric
 100 and magnetic fields, we will briefly tour the various macroscopic populations in the
 101 magnetosphere that are illustrated in Fig. 1.4.

102 The sun and its solar wind are ultimately the source of energy input into the
 103 magnetosphere. The solar wind at Earth's orbit is a plasma traveling at supersonic

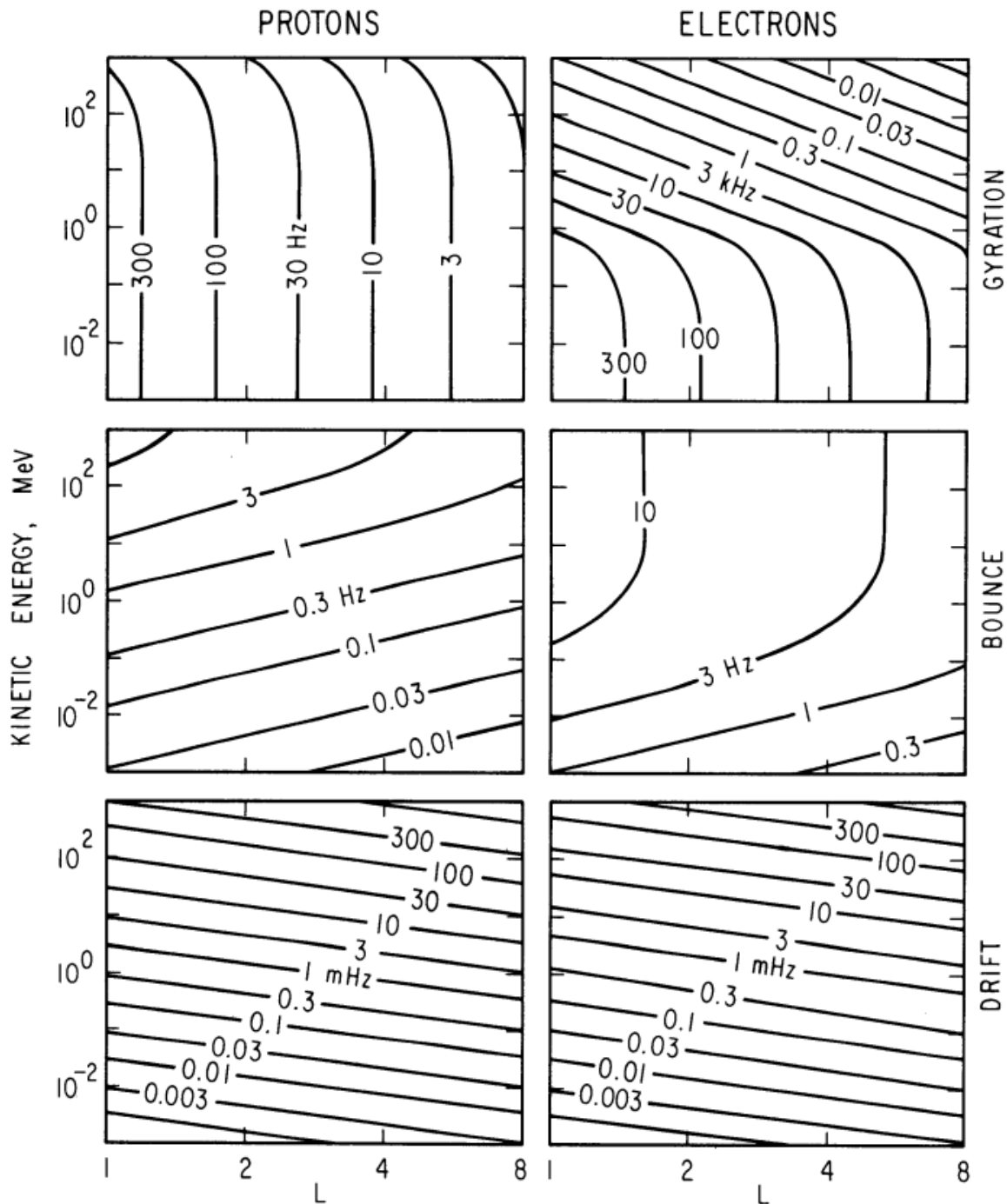


Figure 1.3: Contours of constant gyration, bounce, and drift frequencies for electrons and protons in a dipole field. Figure from Schulz and Lanzerotti (1974).

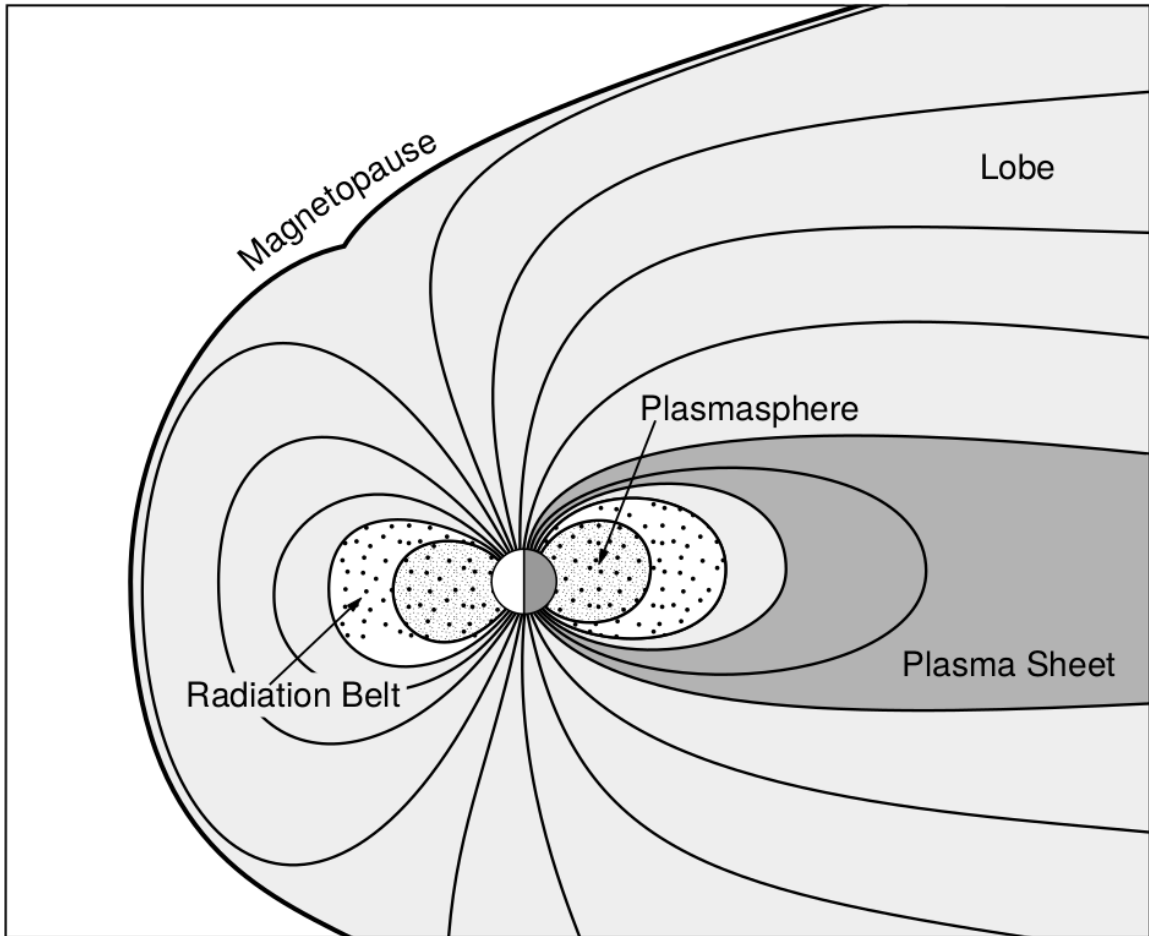


Figure 1.4: A few macroscopic structures in the magnetosphere. The magnetosphere boundary with the solar wind is the magnetopause. The magnetotail consists of two lobes that contain Earth's magnetic flux with the plasma sheet separating the two lobes. The inner magnetosphere contains the plasmasphere, the ring current, and the radiation belts which are co-located. Figure from Baumjohann and Treumann (1997).

speeds with an embedded interplanetary magnetic field (IMF). When the solar wind encounters Earth's magnetic field, the plasma can not easily penetrate into the magnetosphere because the plasma is frozen-in on magnetic field lines. Thus the plasma and its magnetic field drapes around the magnetosphere, forming a cavity in the solar wind that qualitatively has a shape as shown in Fig. 1.4. Because the solar wind is supersonic at 1 AU, a bow shock exists upstream of the magnetosphere. The solar wind plasma, after it is shocked by the bow shock, flows around the magnetosphere inside the magnetosheath. The surface where the solar wind ram pressure and Earth's magnetic pressure balance is termed the magnetopause, which can be thought of as a boundary between the solar wind and Earth's magnetosphere. This is a slightly naive description of the magnetopause, but is nonetheless an instructive conceptual picture. The shocked plasma then flows past the Earth where it shapes the magnetotail. In the magnetotail the magnetopause exists where the solar wind magnetic pressure balances Earth's magnetic field pressure in the lobes. The magnetotail extends on the order of $100 R_E$ downstream of Earth, and the tailward stretching of magnetic field lines creates the plasma sheet which exists in the region of low magnetic field strength near the magnetic equator (e.g. ?).

121 Populations in the Inner Magnetosphere

Closer to Earth, where the magnetic field is largely dipolar, are three plasma populations that comprise the inner magnetosphere: the plasmasphere, the ring current, and the radiation belts which are shown in Fig. 1.4. Before we describe these three particle populations in detail, we will first introduce the coordinate system that most naturally describes the inner magnetosphere environment, and then the electric fields that effect mostly low energy particles.

In this coordinate system the “radial” coordinate was defined in section 1 and

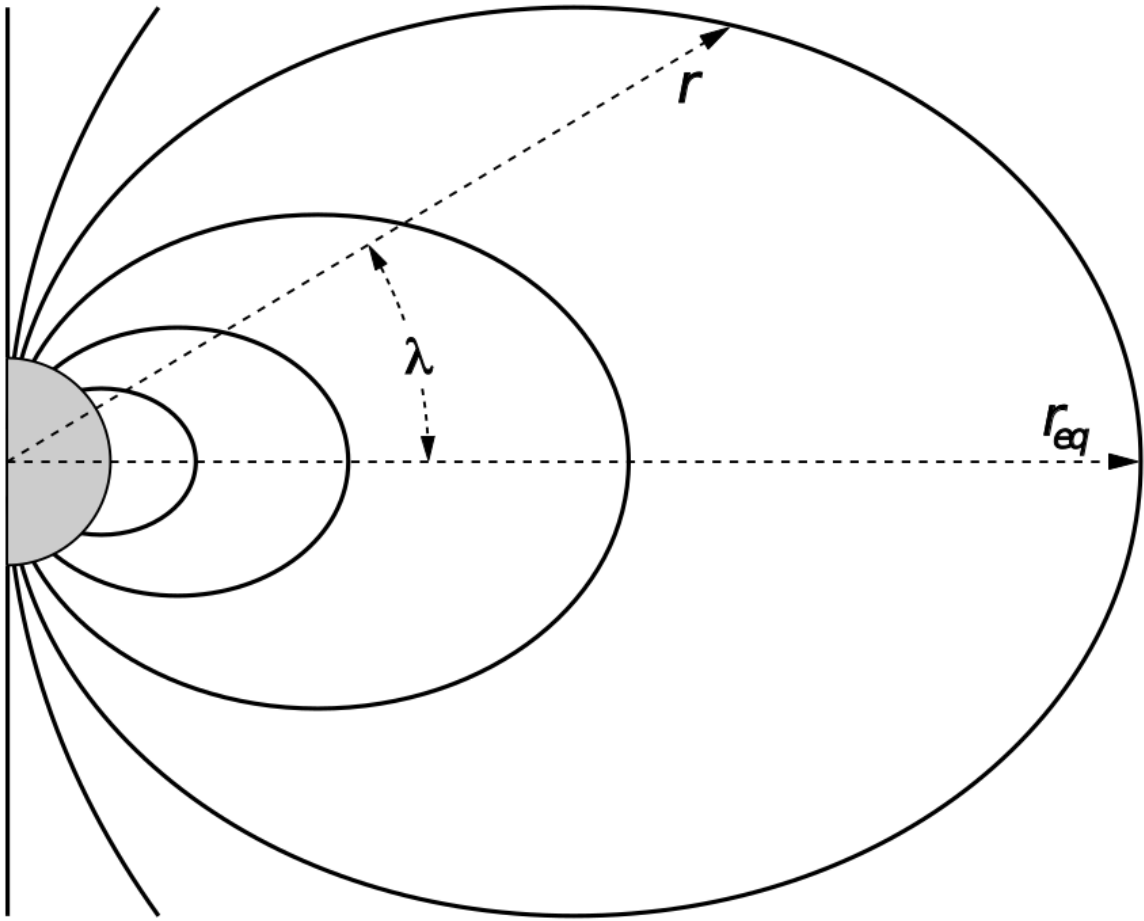


Figure 1.5: The dipole coordinate system. The magnetic latitude of \mathbf{r} is λ . The radial distance to a magnetic field line in the equatorial plane is typically given by $L = r_{eq}/R_e$. Figure from Baumjohann and Treumann (1997).

is the L shell. The azimuthal coordinate is the magnetic local time (MLT). For an observer above Earth's north pole looking down, MLT is defined to be 0 (midnight) in the anti-sunward direction, and increases in the counter-clockwise direction with 6 at dawn, 12 at noon (sunward direction), and 18 in dusk. The final coordinate is the magnetic latitude, λ which is analogous to the latitude coordinate in the spherical coordinate system, and is defined to be 0 at the magnetic equator. This coordinate system is shown in Fig. 1.5 and naturally describes the inner magnetosphere populations described below.

137 The low energy particle dynamics in the inner magnetosphere are organized by
 138 two electric fields: the co-rotation and the dawn-dusk electric fields. The co-rotation
 139 electric field arises from Earth's rotation. The magnetic field and the particles frozen
 140 on it rotate with the Earth. To a non-rotating observer this rotation appears as a
 141 radial electric field that drops off as $\sim L^{-2}$. The other electric field, pointing from
 142 dawn to dusk is called the convection electric field and is due to the Earthward
 143 transport of particles from the magnetotail that appears as an electric field in Earth's
 144 reference frame. The superposition of the co-rotation and convection electric
 145 fields is a potential field shown in Fig. 1.6. The shaded area in Fig. 1.6 shows the
 146 orbits on which low energy electrons are trapped, and outside this region the particles
 147 are not trapped. The dynamic topology of the shaded region in Fig. 1.6 is controlled
 148 by only the convection electric field which is dependent on the solar wind speed and
 149 the IMF. The lowest energy particles that orbit in the shaded region in Fig. 1.6 make
 150 up the plasmasphere.

151 Plasmasphere The plasmasphere is a dense ($n_e \sim 10^3/\text{cm}^3$), cool ($\sim \text{eV}$)
 152 plasma. The plasmasphere typically extends to $L \sim 4$ and the spatial extent is
 153 highly dependent on the solar wind and magnetospheric conditions. The source
 154 of the plasmasphere is the ionosphere. The two main mechanisms that fill the
 155 plasmasphere with cold plasma are ionization of the ionosphere by sunlight and
 156 particle precipitation. The ultraviolet ionization by sunlight is strongly dependent
 157 on the time of day (day vs night), latitude (more ionization near the equator). The
 158 ionization due to particle precipitation, on the other hand, is highly dependent on
 159 magnetospheric conditions, and mostly occurs at high latitudes.

160 The outer boundary of the plasmasphere is the plasmapause which is typically
 161 identified as a steep radial gradient in plasma density from $\sim 10^3/\text{cm}^3$ to $\sim 1/\text{cm}^3$.

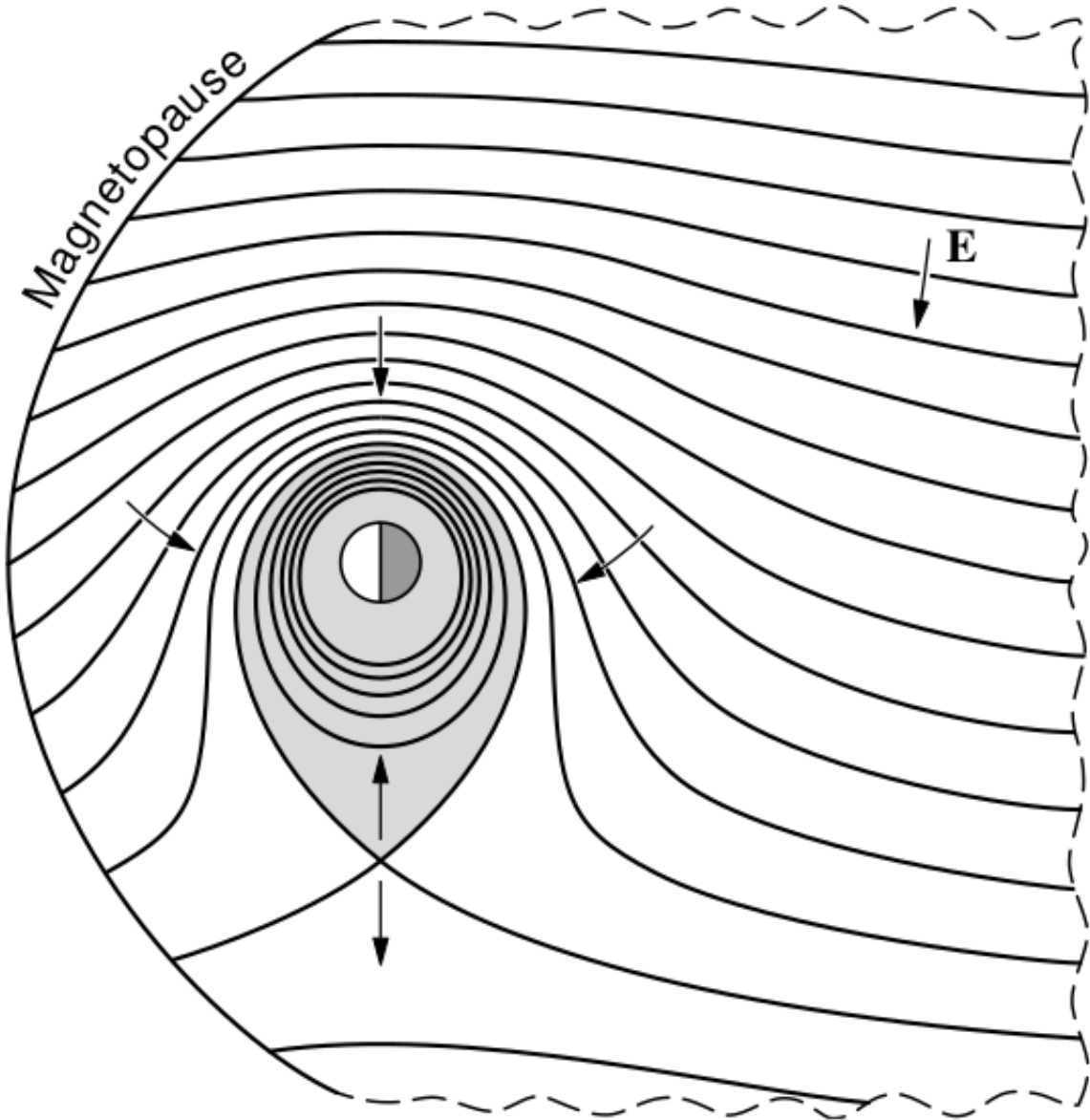


Figure 1.6: Equipotential lines and electric field arrows due to the superposition of the co-rotation and convection electric fields. Electrons in the shaded region execute closed orbits. Outside of the shaded regions the electrons are not trapped and will escape. The region separating the two regimes is called the Alfvén layer. Figure from Baumjohann and Treumann (1997).

162 The location of the plasmapause is important to model (e.g. O'Brien and Moldwin,
163 2003) and understand since the plasma density strongly controls the efficiency of
164 particle scattering by waves (e.g. Horne et al., 2005).

165 Ring Current The next higher energy population is the ring current. This
166 population consists of protons and electrons between tens and a few hundred keV
167 that drift around the Earth. The orbits of higher energy particles are not as effected
168 by the convection and co-rotation electric field, rather they drift around the Earth
169 due to gradient and curvature drifts. Since the direction of the drift is dependent on
170 charge, protons drift west around the Earth and electrons drift East. This has the
171 effect of creating a current around the Earth.

172 The ring current generates a magnetic field which decreases the magnetic field
173 strength at the surface of the Earth and increases it outside of the ring current.
174 The decrease of Earth's magnetic field strength is readily observed by a system of
175 ground-based magnetometers and is merged into a Disturbance Storm Time (DST)
176 index to quantify the global reduction in the magnetic field. An example of a DST
177 index time series from the 2015 St. Patrick's Day storm, driven by a coronal mass
178 ejection (CME), is shown in Fig. 1.7. A few notable features of the storm and the
179 ring current are worth pointing out. At the start of the storm the ring current is
180 sometimes depleted and DST increases slightly (termed the initial phase or sudden
181 storm commencement). Then the ring current population is rapidly built up and
182 DST rapidly decreases during the main phase. Lastly, after the storm passes, the
183 ring current gradually decays toward its equilibrium state over a period of a few
184 days and DST returns towards 0 during the recovery phase. The DST index (along
185 with other geomagnetic indices) are readily used by the space physics community to
186 quantify the global state of the magnetosphere.

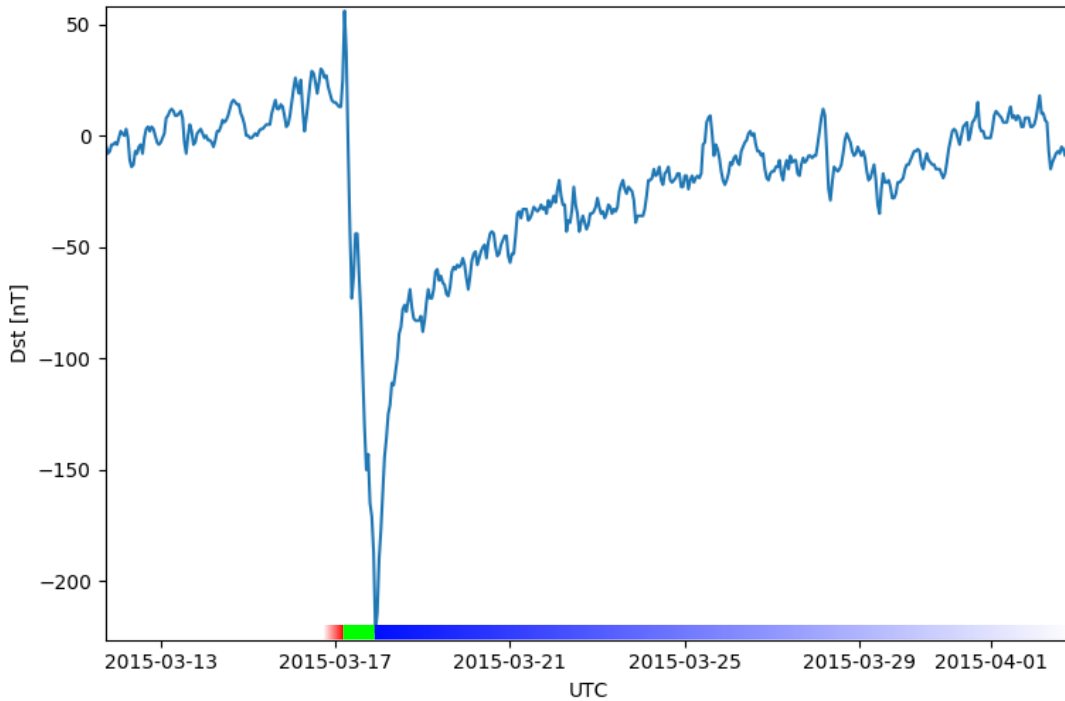


Figure 1.7: The DST index during the St. Patrick's Day 2015 storm. This storm was caused by a coronal mass ejection on March 15th, 2015. The storm phases are: initial phase, main phase, and recovery phase. The initial phase occurred when the Dst peaked at $+50$ nT on March 17th during which the ring current was eroded by the coronal mass ejection during the interval shown by the red bar shown at the bottom. Then the following rapid decrease to ≈ -200 nT was during the main phase where many injections from the magnetotail enhanced the ring current, which reduced Earth's magnetic field strength at the ground, and is shown with the green bar. Lastly, the recovery phase lasted from March 18th to approximately March 29th during which the ring current particles were lost and the ring current returned to its equilibrium state. The recovery phase is shown with the blue bar.

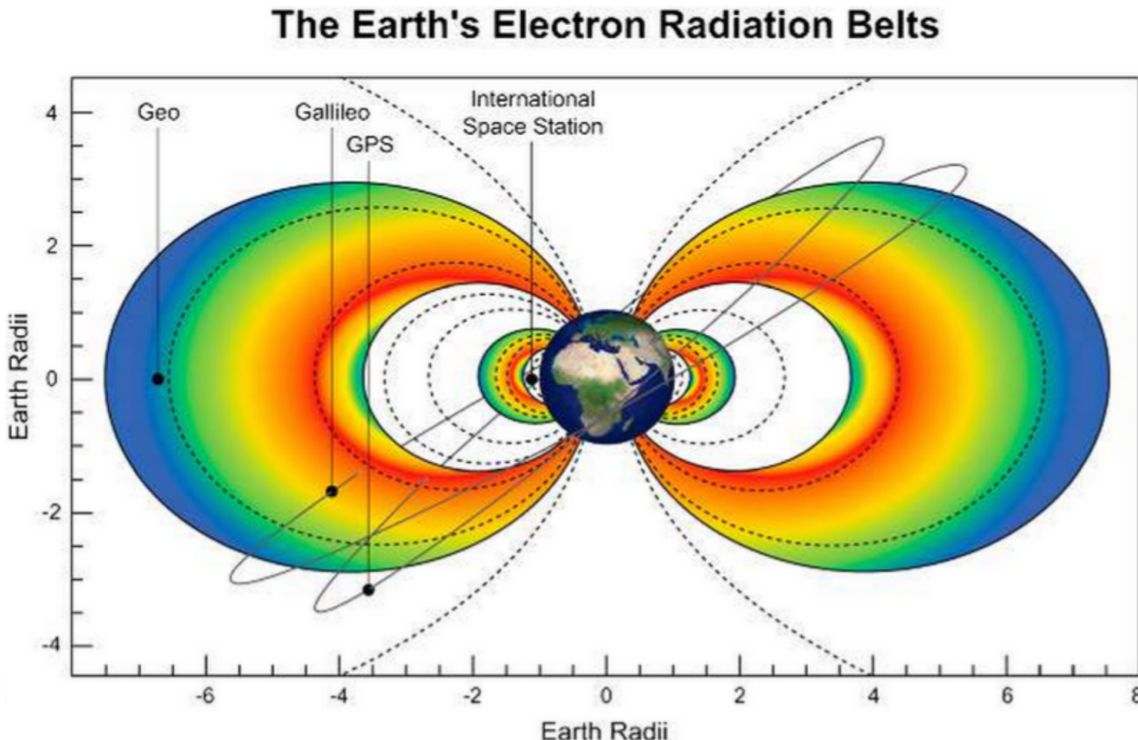


Figure 1.8: The two radiation belts with the locations of various satellites and orbits. Figure from (Horne et al., 2013).

187 Radiation Belts The highest particle energy populations are in the Van Allen
 188 radiation belts. These belts were discovered by Van Allen (1959) and Vernov and
 189 Chudakov (1960) during the Cold War and are a pair of toroidally shaped populations
 190 of trapped electrons and protons shown in Fig. 1.8. Their quiescent toroidal shape,
 191 similar to the shape of the plasmasphere and ring current, is a result of Earth's dipole
 192 magnetic field.

193 The inner radiation belt is extremely stable on time periods of years, extends
 194 to $L \approx 2$, and mainly consists of protons with energies between MeV and GeV and
 195 electrons with energies up to ≈ 1 MeV (Claudepierre et al., 2019). The source of
 196 inner radiation belt protons is believed to be due to cosmic-ray albedo neutron decay
 197 (e.g. Li et al., 2017) and inward radial diffusion for electrons (e.g. O'Brien et al.,

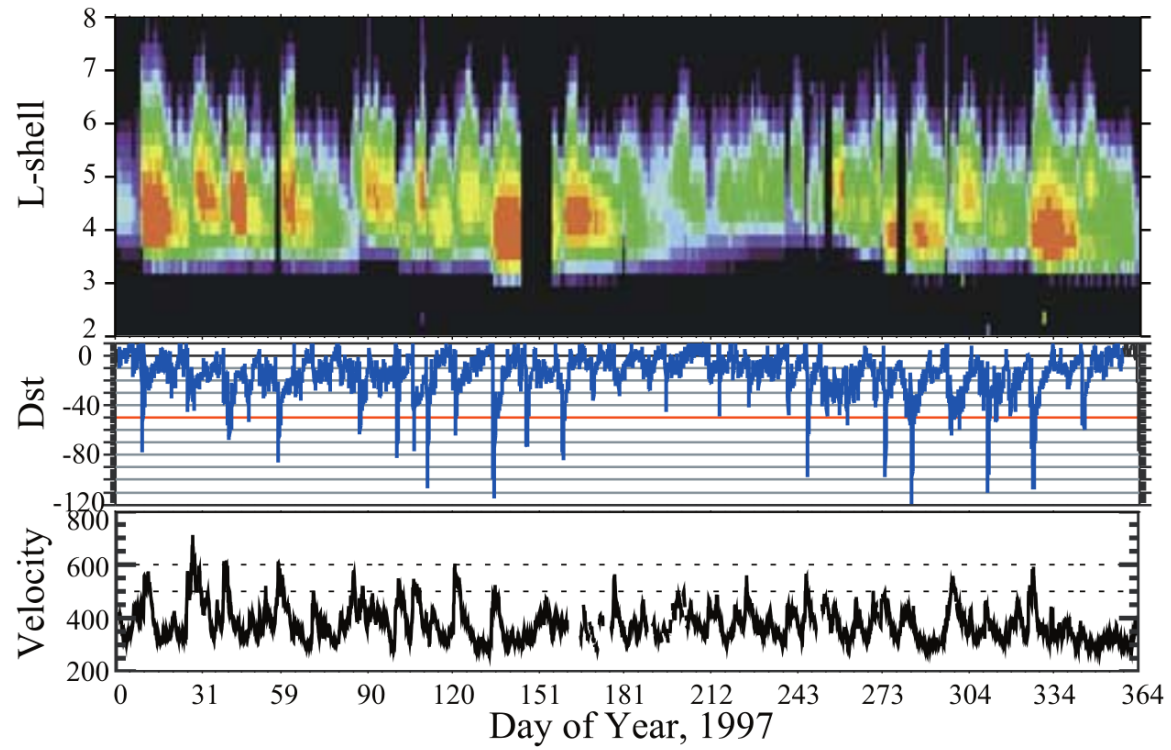


Figure 1.9: The dynamics of the outer radiation belt in 1997 from the POLAR satellite. Top panel shows the 1.2-2.4 MeV electron flux as a function of L and 1997 day of year. The middle panel shows the DST index, and bottom panel shows the solar wind velocity. Figure from (Reeves et al., 2003).

¹⁹⁸ 2016). The gap between the inner and outer radiation belt is called the slot, which is
¹⁹⁹ believed to be due to hiss waves inside the plasmasphere (described below) scattering
²⁰⁰ particles into the atmosphere (e.g. Breneman et al., 2015; Lyons and Thorne, 1973).

²⁰¹ The outer radiation belt is much more dynamic and consists of mainly electrons
²⁰² of energies up to a few MeV. The outer belt's spatial extent is highly variable as
²⁰³ shown in Fig. 1.9, and is typically observed between L of 4 and 8. The source of
²⁰⁴ outer radiation belt electrons is widely believed to be injections of plasma from the
²⁰⁵ magnetotail that is then accelerated to high energies.

²⁰⁶ Due to the highly energetic and dynamic nature of the radiation belts, and their
²⁰⁷ impact on human presence in space, the radiation belts have been studied for over
²⁰⁸ half century. Researchers have studied and attempted to predict the dynamics of
²⁰⁹ radiation belt particles, waves, and wave-particle interactions by considering various
²¹⁰ competing particle acceleration and loss mechanisms which are described next.

²¹¹ Radiation Belt Particle Sources and Sinks

²¹² Adiabatic Heating

²¹³ One of the particle heating and transport mechanisms arises from the Earthward
²¹⁴ convection of particles. The conservation of J_1 implies that the initial and final v_\perp
²¹⁵ depends on the change in the magnetic field amplitude

$$\frac{v_{\perp i}^2}{B_i} = \frac{v_{\perp f}^2}{B_f}. \quad (1.12)$$

²¹⁶ As a particle convects Earthward, $B_f > B_i$ thus v_\perp must increase. The dipole
²¹⁷ magnetic field amplitude can be written as

$$B(L, \theta) = \frac{31.2 \mu\text{T}}{L^3} \sqrt{1 + 3 \cos^2 \theta}. \quad (1.13)$$

₂₁₈ The change in v_{\perp}^2 can be found by taking the ratio of $B(L, \theta)$ at two different L shells

$$\frac{v_{\perp f}^2}{v_{\perp i}^2} = \left(\frac{L_i}{L_f} \right)^3 \quad (1.14)$$

₂₁₉ thus the increase in $v_{\perp} \sim (L_i/L_f)^{3/2}$.

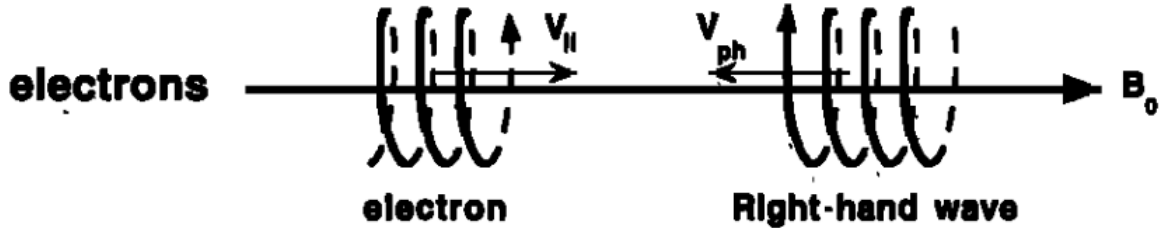
₂₂₀ As the particle convects Earthward its v_{\parallel} also increases because the distance
₂₂₁ between the particle's mirror points decrease. If J_2 is conserved, the shrinking bounce
₂₂₂ path implies that v_{\parallel} must increase by

$$\frac{v_{\parallel f}^2}{v_{\parallel i}^2} = \left(\frac{L_i}{L_f} \right)^k \quad (1.15)$$

₂₂₃ where k ranges from 2 for equatorial pitch angles, $\alpha_{eq} = 0^\circ$, to 2.5 for $\alpha_{eq} = 90^\circ$
₂₂₄ (Baumjohann and Treumann, 1997). Since the rate of adiabatic heating is greater in
₂₂₅ the perpendicular direction than heating in the parallel direction, an initially isotropic
₂₂₆ particle distribution will become anisotropic during its convection. These isotropic
₂₂₇ particles can then become unstable to wave growth and generate waves in order to
₂₂₈ reach equilibrium.

₂₂₉ Wave Resonance Heating

₂₃₀ Another mechanism that heats particles is due to particles resonating with
₂₃₁ plasma waves. A few of the electromagnetic wave modes responsible for particle
₂₃₂ acceleration (and scattering) relevant to radiation belt dynamics are hiss, whistler
₂₃₃ mode chorus (chorus), and electromagnetic ion cyclotron (EMIC) waves. These waves
₂₃₄ are created by the loss cone instability that is driven by an anisotropy of electrons for
₂₃₅ chorus waves, and protons for EMIC waves. The level of anisotropy can be quantified
₂₃₆ by the ratio of the perpendicular to parallel particle temperatures (T_{\perp}/T_{\parallel}). A particle
₂₃₇ distribution is unstable when $T_{\perp}/T_{\parallel} > 1$. Since electrons gyrate in a right-handed



$$\omega + k_{\parallel} v_{\parallel} = \Omega^-$$

Figure 1.10: The trajectories of an electron and a right-hand circularly polarized wave during a cyclotron resonance. The electron's v_{\parallel} and the wave's k_{\parallel} are in opposite directions such that the wave's frequency is Doppler shifted to an integer multiple of the electron cyclotron frequency. Figure from (Tsurutani and Lakhina, 1997).

²³⁸ sense, the chorus waves also tend to be right hand circularly polarized (Tsurutani and
²³⁹ Lakhina, 1997). The same argument also applies to protons and left hand circularly
²⁴⁰ polarized EMIC waves.

²⁴¹ These circularly polarized waves can resonate with electrons and/or protons
²⁴² when their relative motion results in a static \vec{E} . One example of a resonance between
²⁴³ a right hand circularly polarized wave and an electron is shown in Fig. 1.10. The
²⁴⁴ electron's v_{\parallel} and the wave's parallel wave vector, k_{\parallel} are in opposite directions such
²⁴⁵ that the wave frequency ω is Doppler shifted to an integer multiple of the Ω_e where the
²⁴⁶ electron feels a static electric field and is accelerated or decelerated. Quantitatively,
²⁴⁷ this resonance condition is easier to understand with the following toy model.

²⁴⁸ Assume a uniform magnetic field $\vec{B} = B_0 \hat{z}$ with a parallel propagating ($k = k \hat{z}$),
²⁴⁹ right-hand circularly polarized wave. The wave's electric field as a function of position
²⁵⁰ and time can be written as

$$\vec{E} = E_0(\cos(\omega t - kz)\hat{x} + \sin(\omega t - kz)\hat{y}). \quad (1.16)$$

The angular component of \vec{E} that will effect the particle's v_{\perp} is

$$E_{\theta} = \vec{E} \cdot \hat{\theta} = E_0 \cos(\omega t - kz + \theta). \quad (1.17)$$

²⁵¹ Now assume that the electron is traveling in the $-\hat{z}$ direction with a velocity $\vec{v} = -v_0 \hat{z}$

²⁵² so its time dependent position along \hat{z} is

$$z(t) = -v_0 t \quad (1.18)$$

²⁵³ and gyrophase is

$$\theta(t) = -\Omega t + \theta(0) \quad (1.19)$$

²⁵⁴ where the first negative sign comes from the electron's negative charge. Now we put
²⁵⁵ this all together and find the force that the electron will experience

$$m \frac{dv_{\theta}}{dt} = q E_{\theta} = q E_0 \sin((\omega + kv_0 - \Omega)t + \theta(0)). \quad (1.20)$$

²⁵⁶ This is a relatively complex expression, but when the time dependent component is
²⁵⁷ 0, i.e.

$$\omega + kv_0 - \Omega = 0, \quad (1.21)$$

²⁵⁸ the electron will feel a static electric field and be accelerated or decelerated depending
²⁵⁹ on θ_0 , the phase between the wave and the electron. The expression in Eq. 1.21 is
²⁶⁰ commonly referred to as the resonance condition and is more generally written as

$$\omega - k_{||} v_{||} = \frac{n \Omega_e}{\gamma} \quad (1.22)$$

261 where n is the resonance order, and γ is the relativistic correction (e.g. Millan and
 262 Thorne, 2007). In the case of the cyclotron resonance, $\omega \approx \Omega_e$ thus J_1 is violated.
 263 Since J_1 is violated, J_2 and J_3 are also violated since the conditions required to violate
 264 J_2 and J_3 are less stringent than J_1 . It is important to remember that a particle will
 265 experience the effects of many waves along its drift orbit. The typical MLT extent
 266 of a handful of waves that are capable of resonating with radiation belt electrons are
 267 shown in Fig. 1.11.

268 Particle Losses

269 Now that we have seen two general mechanisms with which particles are
 270 accelerated in the magnetosphere, we will now consider a few specific mechanisms
 271 that remove particles from the magnetosphere into the atmosphere or the solar
 272 wind. One mechanism that transports magnetosperic particles into the solar wind
 273 is magnetopause shadowing (e.g. Ukhorskiy et al., 2006). Magnetopause shadowing
 274 occurs when the ring current is strengthened and Earth's magnetic field strength is
 275 increased outside of the ring current. If the ring current increases slowly enough (such
 276 that J_3 is conserved), a particle drift shell will move outward to conserve J_3 . If the
 277 particle's drift shell expands past the magnetopause, the particle will be lost to the
 278 solar wind.

279 **Make sure I understand ULF waves and radial diffusion right** Another particle
 280 loss (and acceleration) mechanism is driven by ultra low frequency (ULF) waves and
 281 is called radial diffusion. Radial diffusion is the transport of particles from high
 282 to low phase space density, f . If the transport is radially inward, particles will
 283 appear to be accelerated. On the other hand, radially outward radial diffusion can
 284 transport particles through the magnetopause where they will be lost to the solar
 285 wind. Reeves et al. (2013) investigated the driver of particle acceleration during the

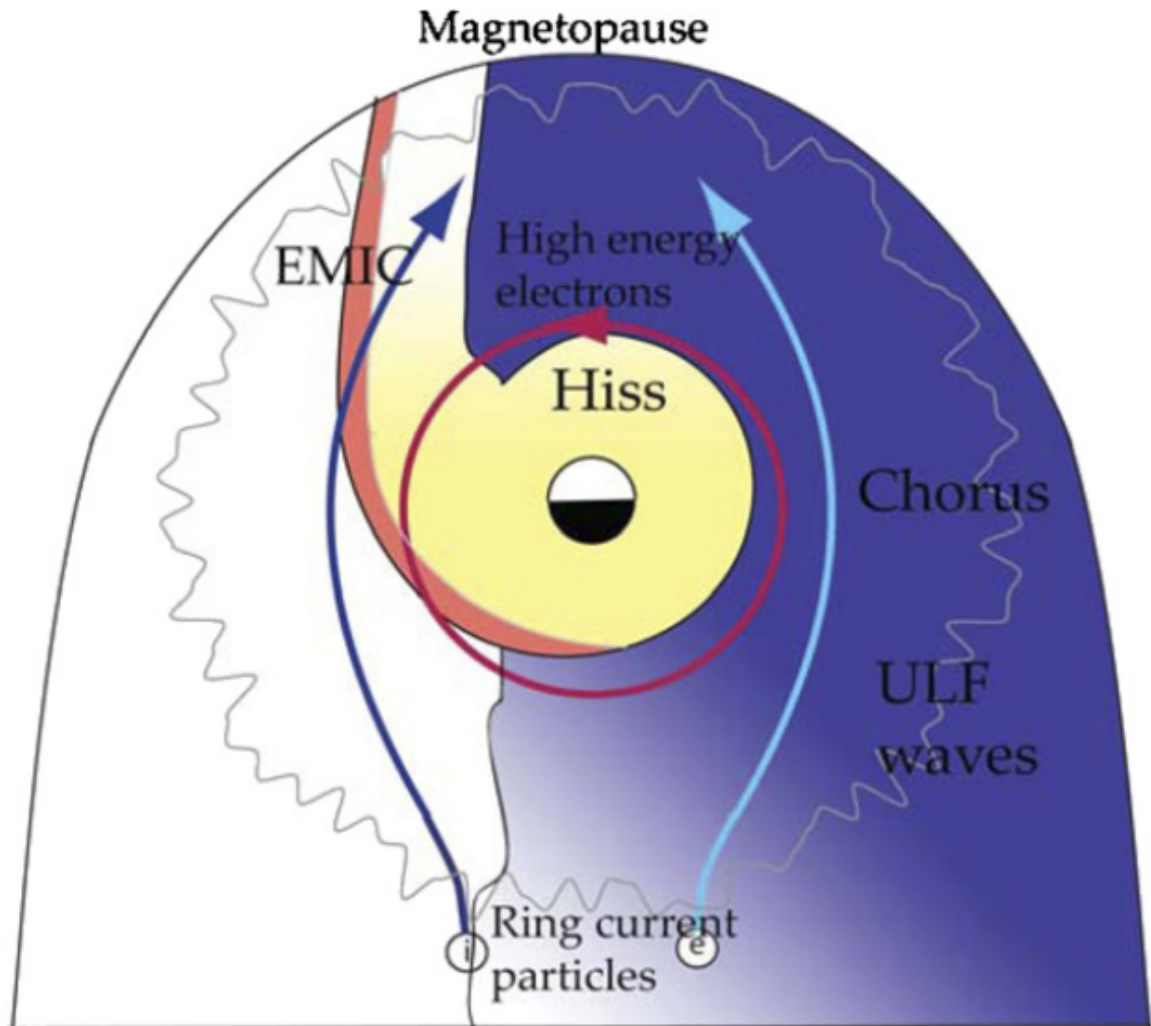


Figure 1.11: Various wave modes in the magnetosphere. Ultra low frequency waves occur through the magnetosphere. Chorus waves are typically observed in the 0-12 midnight-dawn region. EMIC waves are typically observed in the dusk MLT sector. Hiss waves are observed inside the plasmasphere. Figure from Millan and Thorne (2007).

286 October 2012 storm and observationally found that inward radial diffusion was not
 287 dominant, rather local acceleration via wave-resonance heating appeared to be the
 288 dominant acceleration mechanism.

289 The loss mechanism central to this dissertation is pitch angle and energy
 290 scattering of electrons by waves. Some of the waves that scatter electrons in energy
 291 and pitch angle in the inner magnetosphere are: plasmaspheric hiss (e.g. Breneman
 292 et al., 2015; O'Brien et al., 2014), EMIC waves (e.g. Capannolo et al., 2019; Hendry
 293 et al., 2017), and chorus waves (e.g. Breneman et al., 2017; Kasahara et al., 2018;
 294 Ozaki et al., 2019). These wave-particle interactions occur when the resonance
 295 condition in Eq. 1.22 is satisfied and the particle's energy and α is modified by
 296 the wave. More details regarding the theory of pitch angle and energy diffusion is
 297 given in Chapter ???. If the wave changes α towards 0 and $\alpha < \alpha_L$, then the particle's
 298 mirror point dips below 100 km altitude where the particle can be lost from the
 299 magnetosphere. One manifestation of pitch angle scattering of particles into the loss
 300 cone are microbursts: a sub-second durtaison impulse of electrons.

301

Microbursts

302 Microbursts were first with high altitude balloons which measured bremsstrahlung
 303 X-rays emitted by microburst electrons impacting the atmosphere by Anderson
 304 and Milton (1964). In the following years, numerous balloon flights expanded our
 305 knowledge of non-relativistic (≤ 500 keV) microbursts (relativistic microbursts have
 306 not yet been observed by high altitude balloons) by quantifying the microburst
 307 spatial extent, temporal width, occurrence frequency, extent in L and MLT, and
 308 their source. The microburst source was first believed to be either a local plasma
 309 instability or a propagating disturbance in the magnetosphere (Barcus et al., 1966;
 310 Parks, 1967; Trefall et al., 1966; ?). Soon after, both non-relativistic and relativistic

311 microbursts electrons were directly observed in LEO with spacecraft including the
 312 Solar Anomalous and Magnetospheric Particle Explorer (SAMPEX) (e.g. Blake et al.,
 313 1996; Blum et al., 2015; Douma et al., 2017; Greeley et al., 2019; Lorentzen et al.,
 314 2001a,b; Nakamura et al., 1995, 2000; O'Brien et al., 2004, 2003; ?), Montana State
 315 University's (MSU) Focused Investigation of Relativistic Electron Bursts: Intensity,
 316 Range, and Dynamics II (FIREBIRD-II) (Anderson et al., 2017; Breneman et al.,
 317 2017; Crew et al., 2016; ?; ?), and Science Technologies Satellite (STSAT-I) (e.g. Lee
 318 et al., 2012, 2005). An example microburst time series is shown in Fig. 1.12 and was
 319 observed by the FIREBIRD-II CubeSats. The prominent features of the example
 320 microbursts in Fig. 1.12 are their sub-second duration, half order of magnitude
 321 increase in count rate above the falling background, and their 200-800 keV energy
 322 extent.

323 Microbursts are observed on magnetic field footprints that are connected to the
 324 outer radiation belt (approximately $4 < L < 8$). They are predominately observed in
 325 the 0-12 MLT sector with an elevated occurrence frequency during magnetospherically
 326 disturbed times as shown in Fig. 1.13 (e.g. Douma et al., 2017). O'Brien et al. (2003)
 327 used SAMPEX relativistic electron data and found that microbursts predominately
 328 occur during the main phase of storms, with a heightened occurrence rate during the
 329 recovery phase. Microburst occurrence rates are also higher during high solar wind
 330 velocity events e.g. from co-rotating interaction regions (Greeley et al., 2019; O'Brien
 331 et al., 2003).

332 The estimated impact of microbursts on the atmosphere and the radiation belts
 333 is significant. Relativistic microburst electrons impacting the atmosphere are ionized
 334 at < 100 km altitudes, with higher energy electrons penetrating closer to the surface.
 335 The resulting chemical reaction of microburst electrons impacting the atmosphere
 336 produces odd hydrogen HO_x and odd nitrogen NO_x molecules, which are partially

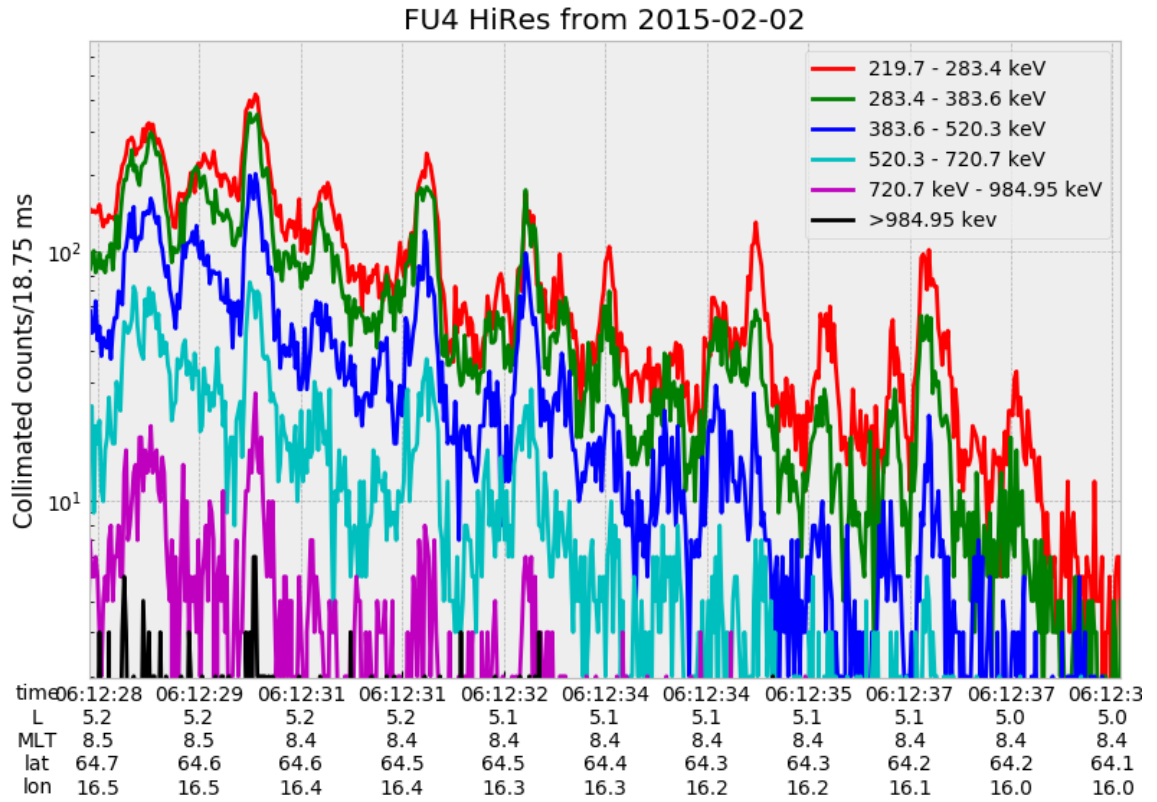


Figure 1.12: An example train of microbursts observed by FIREBIRD-II unit 4 on February 2nd, 2015. The colored curves show the differential energy channel count rates in five channels from ≈ 200 keV to 1 MeV and a sixth integral energy channel with a 1 MeV threshold. The x-axis labels show auxiliary information such as time of observation and the spacecraft position in L, MLT, latitude and longitude coordinates.

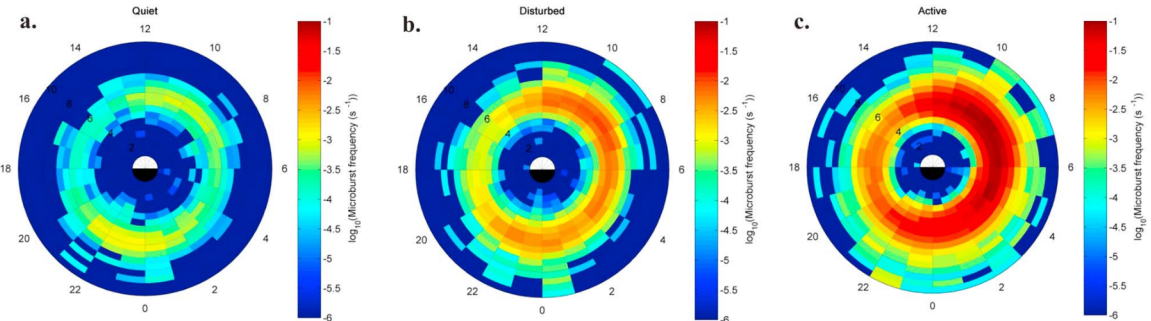


Figure 1.13: Distribution of > 1 MeV microburst occurrence rates as a function of L and MLT. The three panels show the microburst occurrence rate dependence on geomagnetic activity, parameterized by the auroral electrojet (AE) index for (a) $AE < 100$ nT, (b) $100 < AE < 300$ nT and (c) $AE > 300$ nT. Figure from Douma et al. (2017).

337 responsible for destroying ozone (O_3). ? modeled a six hour relativistic microburst
 338 storm and found that the mesospheric ozone was reduced by 7 – 12% in the summer
 339 months and 12 – 20% in the winter months, so microbursts may have a non-negligible
 340 contribution to the dynamics of atmospheric ozone. Furthermore, microbursts have
 341 also been estimated to have a significant impact on the outer radiation belt electron
 342 population. Radiation belt electron loss due to microbursts has been estimated to be
 343 on the order of a day (Breneman et al., 2017; Lorentzen et al., 2001b; O’Brien
 344 et al., 2004; ?; ?).

345 The wave-particle interactions responsible for generating microbursts are also
 346 believed to accelerate electrons in the radiation belts. As mentioned earlier, when
 347 an electron is in resonance with a wave, energy is exchanged with the wave and
 348 the electron is either accelerated or decelerated. The signature of wave-particle
 349 acceleration been observed for radiation belt electrons (e.g. Horne et al., 2005; Reeves
 350 et al., 2013; ?), and O’Brien et al. (2003) presented evidence that enhancements in
 351 chorus waves, microbursts, and radiation belt electrons are related. To explain their
 352 observations, O’Brien et al. (2003) proposed that microburst precipitation is a side

353 effect of electron acceleration due to chorus waves.

354 The widely used theoretical framework to model the wave-particle interactions
 355 responsible for accelerating electrons and scattering microbursts is quasi-linear
 356 diffusion (e.g. Horne et al., 2005; ?; ?; ?; ?; ?). This framework is explained in Chapter
 357 ??, and applied to an observation of a microburst in the heart of the radiation belt.
 358 Qualitatively, when a particle is resonant with a wave it can either be transported in
 359 pitch angle towards the loss cone and lose energy to the wave, or transported away
 360 from the loss cone and gain energy from the wave.

361 As previously mentioned, the range of observed microburst energies range from a
 362 few tens of keV (e.g Datta et al., 1997; Parks, 1967) to greater than 1 MeV (e.g. Blake
 363 et al., 1996; Greeley et al., 2019). The microburst electron flux (J) falls off in energy,
 364 and the microburst energy spectra is typically well fit to a decaying exponential

$$J(E) = J_0 e^{-E/E_0} \quad (1.23)$$

365 where J_0 is the flux at 0 keV (unphysical free parameter) and E_0 quantifies the
 366 efficiency of the scattering mechanism in energy (e.g. Datta et al., 1997; Lee et al.,
 367 2005; Parks, 1967). A small E_0 suggests that mostly low energy particles are scattered.
 368 In contrast a high E_0 suggests that the scattering mechanism scatters low and high
 369 energy electrons. Reality is a bit more messy and a high E_0 may be a signature of
 370 a scattering mechanism preferential to high energy electrons, but is hidden by the
 371 convolution of the source particles available to be scattered (typically with a falling
 372 energy spectrum) and the energy-dependent efficiency of the scattering mechanism.

373 The short microburst duration observed by a single LEO satellite has an
 374 ambiguity when interpreting what is exactly a microburst. The two possible realities
 375 are: a microburst is very small and spatially stationary so that the LEO spacecraft

376 passes through it in less than a second. Alternatively, microbursts are spatially large
 377 and transient so a microburst will pass by the spacecraft in a fraction of a second.
 378 There are a few ways to distinguish between the two possible realities, and each one
 379 has a unique set of advantages.

380 A high altitude balloon provides essentially a stationary view of the precipitating
 381 particles under the radiation belt footprints. A short-lived, temporal microburst can
 382 be unambiguously identified. Spatial structures, on the other hand, are difficult to
 383 identify because a balloon is essentially still on drift timescales.

384 Multi-spacecraft missions are an alternate solution that can determine if a
 385 microburst is spatial or temporal. As will be shown in this dissertation, if a microburst
 386 is observed simultaneously by two spacecraft then it is temporal and has a size
 387 greater than the spacecraft separation. On the contrary, if two spacecraft observe
 388 a microburst-like feature at different times but at the same location, then the feature
 389 is spatial and may be a curtain (Blake and O'Brien, 2016). Both balloon and multi-
 390 spacecraft observational methods have a unique set of strengths, and this dissertation
 391 takes the multi-spacecraft approach to identify and study microbursts.

392

Scope of Research

393 This dissertation furthers our understanding of the microburst scattering
 394 mechanism by presenting observational evidence of microburst scattering directly, and
 395 measuring microburst sizes and comparing them to the size of chorus waves. Chapter
 396 ?? (chapter numbers will be filled in the full dissertation) describes a microburst
 397 scattering event observed by NASA's Van Allen Probes. For this event, particle
 398 and wave measurements were analyzed and modeled in the theoretical framework
 399 of pitch angle and energy diffusion. Then the following two chapters present
 400 studies of microburst sizes in comparison to chorus waves. Chapter ?? describes a

401 bouncing packet microburst observation made by the FIREBIRD-II mission where
402 the microburst's lower bound longitudinal and latitudinal sizes were estimated.
403 Then Chapter ?? expands the case study from Chapter ?? to a statistical study
404 of microburst sizes using The Aerospace Corporation's AeroCube-6 (AC6) CubeSats.
405 In this study, a Monte Carlo and analytic microburst size models were developed
406 to account for the compounding statistical effects of random microburst sizes and
407 locations. Lastly, Chapter ?? will summarize this work and make concluding remarks
408 regarding outstanding questions in microburst physics.

Bibliography

- 410 Anderson, B., Shekhar, S., Millan, R., Crew, A., Spence, H., Klumpar, D., Blake, J.,
 411 O'Brien, T., and Turner, D. (2017). Spatial scale and duration of one microburst
 412 region on 13 August 2015. *Journal of Geophysical Research: Space Physics*.
- 413 Anderson, K. A. and Milton, D. W. (1964). Balloon observations of X rays in the
 414 auroral zone: 3. High time resolution studies. *Journal of Geophysical Research*,
 415 69(21):4457–4479.
- 416 Barcus, J., Brown, R., and Rosenberg, T. (1966). Spatial and temporal character of
 417 fast variations in auroral-zone x rays. *Journal of Geophysical Research*, 71(1):125–
 418 141.
- 419 Baumjohann, W. and Treumann, R. A. (1997). *Basic space plasma physics*. World
 420 Scientific.
- 421 Blake, J.,Looper, M., Baker, D., Nakamura, R., Klecker, B., and Hovestadt, D.
 422 (1996). New high temporal and spatial resolution measurements by sampex of the
 423 precipitation of relativistic electrons. *Advances in Space Research*, 18(8):171 – 186.
- 424 Blake, J. B. and O'Brien, T. P. (2016). Observations of small-scale latitudinal
 425 structure in energetic electron precipitation. *Journal of Geophysical Research: Space
 426 Physics*, 121(4):3031–3035. 2015JA021815.
- 427 Blum, L., Li, X., and Denton, M. (2015). Rapid MeV electron precipitation as
 428 observed by SAMPEX/HILT during high-speed stream-driven storms. *Journal of
 429 Geophysical Research: Space Physics*, 120(5):3783–3794. 2014JA020633.
- 430 Breneman, A., Crew, A., Sample, J., Klumpar, D., Johnson, A., Agapitov, O.,
 431 Shumko, M., Turner, D., Santolik, O., Wygant, J., et al. (2017). Observations
 432 directly linking relativistic electron microbursts to whistler mode chorus: Van allen
 433 probes and FIREBIRD II. *Geophysical Research Letters*.
- 434 Breneman, A. W., Halford, A., Millan, R., McCarthy, M., Fennell, J., Sample, J.,
 435 Woodger, L., Hospodarsky, G., Wygant, J. R., Cattell, C. A., et al. (2015). Global-
 436 scale coherence modulation of radiation-belt electron loss from plasmaspheric hiss.
 437 *Nature*, 523(7559):193.
- 438 Brown, R., Barcus, J., and Parsons, N. (1965). Balloon observations of auroral zone
 439 x rays in conjugate regions. 2. microbursts and pulsations. *Journal of Geophysical
 440 Research (U.S.)*.
- 441 Capannolo, L., Li, W., Ma, Q., Shen, X.-C., Zhang, X.-J., Redmon, R., Rodriguez,
 442 J., Engebretson, M., Kletzing, C., Kurth, W., et al. (2019). Energetic electron
 443 precipitation: multi-event analysis of its spatial extent during emic wave activity.
 444 *Journal of Geophysical Research: Space Physics*.

- 445 Claudepierre, S., O'Brien, T.,Looper, M., Blake, J., Fennell, J., Roeder, J.,
 446 Clemmons, J., Mazur, J., Turner, D., Reeves, G., et al. (2019). A revised look
 447 at relativistic electrons in the earth's inner radiation zone and slot region. *Journal*
 448 of *Geophysical Research: Space Physics*, 124(2):934–951.
- 449 Crew, A. B., Spence, H. E., Blake, J. B., Klumpar, D. M., Larsen, B. A., O'Brien,
 450 T. P., Driscoll, S., Handley, M., Legere, J., Longworth, S., Mashburn, K.,
 451 Mosleh, E., Ryhajlo, N., Smith, S., Springer, L., and Widholm, M. (2016). First
 452 multipoint in situ observations of electron microbursts: Initial results from the
 453 NSF FIREBIRD II mission. *Journal of Geophysical Research: Space Physics*,
 454 121(6):5272–5283. 2016JA022485.
- 455 Datta, S., Skoug, R., McCarthy, M., and Parks, G. (1997). Modeling of microburst
 456 electron precipitation using pitch angle diffusion theory. *Journal of Geophysical*
 457 *Research: Space Physics*, 102(A8):17325–17333.
- 458 Douma, E., Rodger, C. J., Blum, L. W., and Clilverd, M. A. (2017). Occurrence
 459 characteristics of relativistic electron microbursts from SAMPEX observations.
 460 *Journal of Geophysical Research: Space Physics*, 122(8):8096–8107. 2017JA024067.
- 461 Dungey, J. W. (1961). Interplanetary magnetic field and the auroral zones. *Phys.*
 462 *Rev. Lett.*, 6:47–48.
- 463 Greeley, A., Kanekal, S., Baker, D., Klecker, B., and Schiller, Q. (2019). Quantifying
 464 the contribution of microbursts to global electron loss in the radiation belts. *Journal*
 465 of *Geophysical Research: Space Physics*.
- 466 Hendry, A. T., Rodger, C. J., and Clilverd, M. A. (2017). Evidence of sub-mev
 467 emic-driven electron precipitation. *Geophysical Research Letters*, 44(3):1210–1218.
- 468 Horne, R., Glauert, S., Meredith, N., Boscher, D., Maget, V., Heynderickx, D., and
 469 Pitchford, D. (2013). Space weather impacts on satellites and forecasting the earth's
 470 electron radiation belts with spacecast. *Space Weather*, 11(4):169–186.
- 471 Horne, R. B., Thorne, R. M., Shprits, Y. Y., Meredith, N. P., Glauert, S. A., Smith,
 472 A. J., Kanekal, S. G., Baker, D. N., Engebretson, M. J., Posch, J. L., et al.
 473 (2005). Wave acceleration of electrons in the van allen radiation belts. *Nature*,
 474 437(7056):227.
- 475 Kasahara, S., Miyoshi, Y., Yokota, S., Mitani, T., Kasahara, Y., Matsuda, S.,
 476 Kumamoto, A., Matsuoka, A., Kazama, Y., Frey, H., et al. (2018). Pulsating
 477 aurora from electron scattering by chorus waves. *Nature*, 554(7692):337.
- 478 Lee, J. J., Parks, G. K., Lee, E., Tsurutani, B. T., Hwang, J., Cho, K. S., Kim, K.-H.,
 479 Park, Y. D., Min, K. W., and McCarthy, M. P. (2012). Anisotropic pitch angle
 480 distribution of 100 keV microburst electrons in the loss cone: measurements from
 481 STSAT-1. *Annales Geophysicae*, 30(11):1567–1573.

- 482 Lee, J.-J., Parks, G. K., Min, K. W., Kim, H. J., Park, J., Hwang, J., McCarthy,
 483 M. P., Lee, E., Ryu, K. S., Lim, J. T., Sim, E. S., Lee, H. W., Kang, K. I., and
 484 Park, H. Y. (2005). Energy spectra of 170–360 keV electron microbursts measured
 485 by the korean STSAT-1. *Geophysical Research Letters*, 32(13). L13106.
- 486 Li, X., Selesnick, R., Schiller, Q., Zhang, K., Zhao, H., Baker, D. N., and Temerin,
 487 M. A. (2017). Measurement of electrons from albedo neutron decay and neutron
 488 density in near-earth space. *Nature*, 552(7685):382.
- 489 Lorentzen, K. R., Blake, J. B., Inan, U. S., and Bortnik, J. (2001a). Observations
 490 of relativistic electron microbursts in association with VLF chorus. *Journal of
 491 Geophysical Research: Space Physics*, 106(A4):6017–6027.
- 492 Lorentzen, K. R.,Looper, M. D., and Blake, J. B. (2001b). Relativistic electron
 493 microbursts during the GEM storms. *Geophysical Research Letters*, 28(13):2573–
 494 2576.
- 495 Lyons, L. R. and Thorne, R. M. (1973). Equilibrium structure of radiation belt
 496 electrons. *Journal of Geophysical Research*, 78(13):2142–2149.
- 497 Millan, R. and Thorne, R. (2007). Review of radiation belt relativistic electron losses.
 498 *Journal of Atmospheric and Solar-Terrestrial Physics*, 69(3):362 – 377.
- 499 Nakamura, R., Baker, D. N., Blake, J. B., Kanekal, S., Klecker, B., and Hovestadt,
 500 D. (1995). Relativistic electron precipitation enhancements near the outer edge of
 501 the radiation belt. *Geophysical Research Letters*, 22(9):1129–1132.
- 502 Nakamura, R., Isowa, M., Kamide, Y., Baker, D., Blake, J., and Looper, M. (2000).
 503 Observations of relativistic electron microbursts in association with VLF chorus.
 504 *J. Geophys. Res*, 105:15875–15885.
- 505 O'Brien, T., Claudepierre, S., Blake, J., Fennell, J. F., Clemons, J., Roeder, J.,
 506 Spence, H. E., Reeves, G., and Baker, D. (2014). An empirically observed pitch-
 507 angle diffusion eigenmode in the earth's electron belt near $l^* = 5.0$. *Geophysical
 508 Research Letters*, 41(2):251–258.
- 509 O'Brien, T., Claudepierre, S., Guild, T., Fennell, J., Turner, D., Blake, J., Clemons,
 510 J., and Roeder, J. (2016). Inner zone and slot electron radial diffusion revisited.
 511 *Geophysical Research Letters*, 43(14):7301–7310.
- 512 O'Brien, T. and Moldwin, M. (2003). Empirical plasmapause models from magnetic
 513 indices. *Geophysical Research Letters*, 30(4).
- 514 O'Brien, T. P., Looper, M. D., and Blake, J. B. (2004). Quantification of relativistic
 515 electron microburst losses during the GEM storms. *Geophysical Research Letters*,
 516 31(4). L04802.

- 517 O'Brien, T. P., Lorentzen, K. R., Mann, I. R., Meredith, N. P., Blake, J. B., Fennell,
 518 J. F., Looper, M. D., Milling, D. K., and Anderson, R. R. (2003). Energization of
 519 relativistic electrons in the presence of ULF power and MeV microbursts: Evidence
 520 for dual ULF and VLF acceleration. *Journal of Geophysical Research: Space
 521 Physics*, 108(A8).
- 522 Ozaki, M., Miyoshi, Y., Shiokawa, K., Hosokawa, K., Oyama, S.-i., Kataoka, R.,
 523 Ebihara, Y., Ogawa, Y., Kasahara, Y., Yagitani, S., et al. (2019). Visualization of
 524 rapid electron precipitation via chorus element wave-particle interactions. *Nature
 525 communications*, 10(1):257.
- 526 Parks, G. K. (1967). Spatial characteristics of auroral-zone X-ray microbursts. *Journal
 527 of Geophysical Research*, 72(1):215–226.
- 528 Reeves, G., Spence, H. E., Henderson, M., Morley, S., Friedel, R., Funsten, H., Baker,
 529 D., Kanekal, S., Blake, J., Fennell, J., et al. (2013). Electron acceleration in the
 530 heart of the van allen radiation belts. *Science*, 341(6149):991–994.
- 531 Reeves, G. D., McAdams, K. L., Friedel, R. H. W., and O'Brien, T. P. (2003). Ac-
 532 celeration and loss of relativistic electrons during geomagnetic storms. *Geophysical
 533 Research Letters*, 30(10):n/a–n/a. 1529.
- 534 Schulz, M. and Lanzerotti, L. J. (1974). *Particle Diffusion in the Radiation Belts*.
 535 Springer.
- 536 Trefall, H., Bjordal, J., Ullaland, S., and Stadsnes, J. (1966). On the extension of
 537 auroral-zone x-ray microbursts. *Journal of Atmospheric and Terrestrial Physics*,
 538 28(2):225–233.
- 539 Tsurutani, B. T. and Lakhina, G. S. (1997). Some basic concepts of wave-particle
 540 interactions in collisionless plasmas. *Reviews of Geophysics*, 35(4):491–501.
- 541 Turner, D., Claudepierre, S., Fennell, J., O'Brien, T., Blake, J., Lemon, C.,
 542 Gkioulidou, M., Takahashi, K., Reeves, G., Thaller, S., et al. (2015). Energetic
 543 electron injections deep into the inner magnetosphere associated with substorm
 544 activity. *Geophysical Research Letters*, 42(7):2079–2087.
- 545 Ukhorskiy, A. Y., Anderson, B. J., Brandt, P. C., and Tsyganenko, N. A. (2006).
 546 Storm time evolution of the outer radiation belt: Transport and losses. *Journal of
 547 Geophysical Research: Space Physics*, 111(A11):n/a–n/a. A11S03.
- 548 Van Allen, J. A. (1959). The geomagnetically trapped corpuscular radiation. *Journal
 549 of Geophysical Research*, 64(11):1683–1689.
- 550 Vernov, S. and Chudakov, A. (1960). Investigation of radiation in outer space. In
 551 *International Cosmic Ray Conference*, volume 3, page 19.

- 552 Woodger, L., Halford, A., Millan, R., McCarthy, M., Smith, D., Bowers, G., Sample,
553 J., Anderson, B., and Liang, X. (2015). A summary of the BARREL campaigns:
554 Technique for studying electron precipitation. *Journal of Geophysical Research:*
555 *Space Physics*, 120(6):4922–4935.